Texas A&M University

Mechanical Engineering Department

Turbomachinery Laboratory

IDENTIFICATION OF STRUCTURAL STIFFNESS AND DAMPING IN A SHOED BRUSH SEAL

Research Progress Report to the Turbomachinery Laboratory

TRC-SEAL-3-05

by

Adolfo Delgado

Research Assistant

Luis San Andrés

Principal Investigator

May 2005

TEES Project Number # 32525/1519S7/ME

EXECUTIVE SUMMARY

The multiple-shoe brush seal, a variation of a standard brush seal, accommodates arcuate pads at the bristles free ends. This novel design allows reverse shaft rotation operation, and reduces and even eliminates bristle wear, since the pads lift off due to the generation of a hydrodynamic film during rotor spinning. This type of seal, able to work at both cold and high temperatures, not only restricts secondary leakage but also acts as an effective vibration damper. The dynamic operation of the shoed-brush seals, along with the validation of reliable predictive tools, relies on the appropriate estimation of the seal structural stiffness and energy dissipation features. Single frequency external load tests conducted on a controlled motion test rig and without shaft rotation allow the identification of the structural stiffness and equivalent damping of a 20-pad brush seal, 153 mm in diameter. The seal energy dissipation mechanism, represented by a structural loss factor and a dry friction coefficient, characterizes the energy dissipated by the bristles and the dry friction interaction of the brush seal bristles rubbing against each other. The physical model used reproduces well the measured system motions, even for frequencies well above the identification range.

Measurements of the leakage through the seal as the supply pressure increases (pressure ratio =3.4) show the seal unique performance characteristics, i.e. very small flow rate (laminar flow) which can be effectively represented as a “labyrinth seal” of very narrow clearance. Model predictions agree reasonably well with the flow measurements.

IDENTIFICATION OF STRUCTURAL STIFFNESS AND DAMPING IN A SHOED BRUSH SEAL

TRC-SEAL-3-05

TABLE OF CONTENTS

LIST OF TABLES

LIST OF FIGURES

NOMENCLATURE

A	Shaft cross-sectional area (127 mm^2)
A_u	Seal area upstream, $=(\pi/4)*(D_u^2-D_j^2)$ [m^2]
B	Brush seal effective film thickness [m]
c_E	Equivalent « labyrinth seal » clearance for brush seal [m]
C_{eq}	System equivalent viscous damping coefficient [N.s/m]
D_J, D_u	Rotor diameter and upstream seal diameter [m]
E_{dis}	Energy dissipated in one period of forced motion [J]
F_{ext}	Excitation force [N]
K_{eq}	Equivalent stiffness for test system [N/m]
K_{shaft}	Shaft stiffness [N/m]
K_s	Brush seal structural stiffness
L	Shaft length [0.248 m]
$\dot{m}$	Seal leakage [g/s]
M_{eq}	System equivalent mass [kg]
M_D	Disk mass [1.36 kg]
P_u, P_d	Upstream (supply) & downstream (discharge) absolute pressures [Pa]
p_r	P_u / P_d , pressure ratio
r	ω/ω_n. Frequency ratio
x	Displacement [m]
T_u	Upstream (supply) temperature [ºC]
t	Time [s]
z	Axial coordinate along shaft [m]
γ_{eq},γ_s	Structural loss coefficient, equivalent and brush seal
μ	Brush seal dry friction coefficient
γ	Gas ratio of specific heats
ρ	Shaft density (7,800 kg/m^3)
φ	Orifice flow factor, Eqn. (14)
Φ	Brush seal flow factor, Eqn. (12)
$\psi(z)$	Shape function of cantilever beam due to a static load
ω	Excitation frequency [rad/s]
ω_n	$(K_{eq}/M_{eq})^{1/2}$, system natural frequency [rad/s]

Complex variables

F	Synchronous component of force
X	Synchronous component of displacement
Z	**F/X**, Impedance function

Subscripts

eq	Equivalent system: shaft + disk + brush seal
f	measurement axial location, load action
s	Seal and disk axial location

INTRODUCTION

Improvements in air-breathing turbomachinery efficiency can be realized with reliable (and predictable) sealing technology. Brush seals have better leakage performance than labyrinth seals [1], require less axial space and are also able to handle larger vibrations [2]. Furthermore, experimental evidence shows that brush seals exhibit favorable rotordynamic characteristics when compared to labyrinth seals, for example [3, 4].

However, premature wear and limitations in sealing pressure differentials have confined brush seals for usage in hybrid configurations, where brush seals are intercalated between labyrinth seals [5]. These configurations take advantage of the brush seal superior leakage performance, but spare the axial space reduction and favorable vibration characteristics associated with brush seals. Furthermore, a brush seal can accommodate shaft rotations in only one direction, thus preventing its use in certain aircraft engine applications.

Justak [6] introduced a novel brush seal design that incorporates metal pads at the bristles' free end, see Figure 1. This modification allows reverse shaft rotation operation and also significantly reduces or eliminates wear, since each individual pad lifts due to a hydrodynamic fluid film wedge induced by rotor spinning. Justak [7] conducted experimental work demonstrating the favorable leakage performance of a shoed brush seal when compared to a conventional brush seal. Delgado *et al.* [8] present a model and measurements to determine the static structural stiffness coefficient of a large diameter (279 mm) shoed brush seal. The experiments evidenced the influence of dry friction, arising from bristle-to-bristle and bristle-to-back plate interactions, on the damping characteristics of the test seal.

Delgado *et al.* [9] present a comprehensive analysis for prediction of the rotordynamic force coefficients in a shoe-brush seal. The model couples the gas film forces generated in the thin gap between the rotor and a shoe and the structural characteristics (stiffness and damping) from the bristle bed underneath. The predictions indicate that the overall stiffness and damping coefficients from a shoed brush are not affected by either the operating gas film clearance or the supply to discharge pressure ratio. On the other hand, direct stiffness drops rapidly with increasing operating shaft speeds. The predictions for damping rely on the appropriate physical characterization of the energy dissipation in the bristle bed and modeled as a hysteretic (structural) damping type. In the theoretical study, the hysteretic (loss) factor varies over a certain range since there is no experimental data was readily available.

The report describes a test rig to perform leakage measurements and dynamic load experiments in brush seals and presents a simple identification method to obtain the seal structural stiffness and damping characteristics. The test data, needed to validate predictive models of brush seal performance, brings forward this novel seal technology.

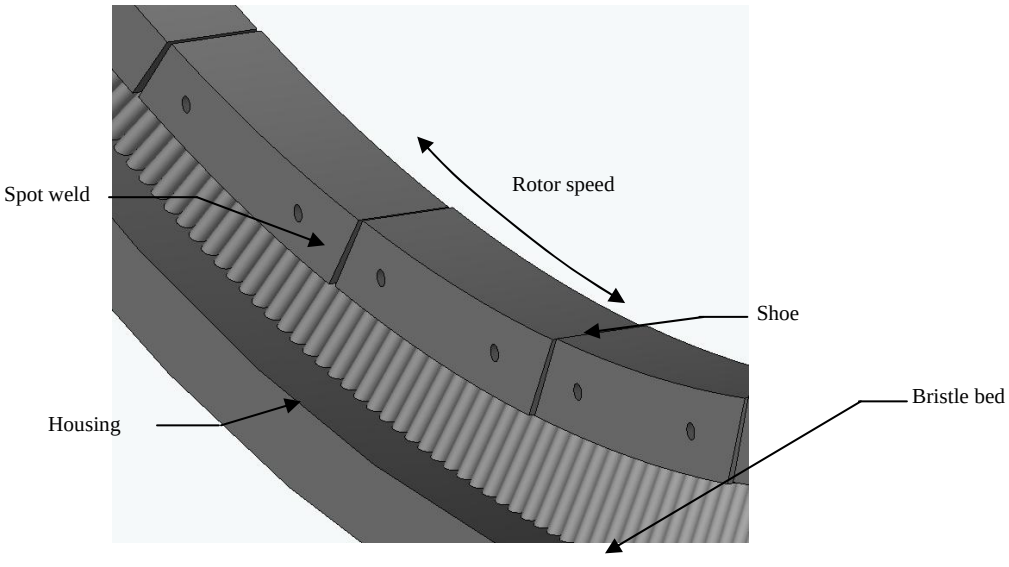

Fig. 1 Close-up view of a shoed-brush seal

TEST RIG DESCRIPTION

Figure 2 shows a cross section view of the test rig. A long and slender steel shaft (12.7 mm in diameter) and an aluminum disk mounted at the shaft end are located inside a cylindrical, thick wall, steel vessel. The disk diameter and thickness equal 163 mm and 25.4 mm, respectively. One end of the shaft is affixed into the bottom of the vessel with two rolling element bearings. The test brush seal is secured at the top of the vessel with an interference fit to the disk.

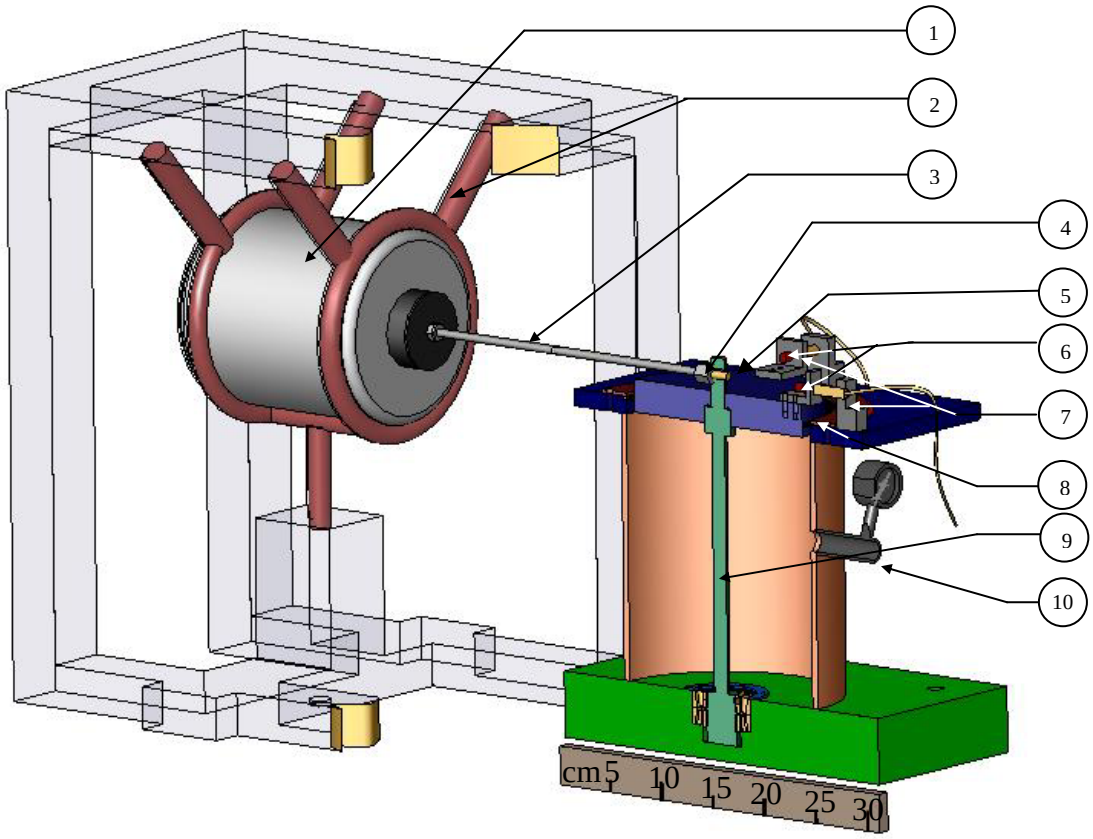

Fig. 2 Cut view of brush seal test rig

1	Electromagnetic Shaker	6	Accelerometers
2	Soft supports (rubber cords)	7	Targets and displacement sensors
3	Stinger	8	Shoed brush seal
4	Load Cell	9	Cantilever shaft
5	Solid Disk	10	Air inlet

Thus, the simple test system comprises of a cantilever beam whose free end carries a large inertia (disk) and the test seal element, which offers stiffness and damping connections to ground. The cylindrical vessel can be pressurized to conduct leakage measurements through the test seal.

A piezoelectric load cell and long stinger connect the end of the shaft to an electromagnetic shaker, softly supported from rubber cords. Two small brackets, 90 ° apart, are mounted on the outer diameter of the solid disk. Two eddy current sensors, installed atop the vessel and facing the brackets, record the disk displacements. Two piezoelectric accelerometers, attached to the brackets, record the disk acceleration in along two orthogonal directions on the horizontal plane. Table 1 lists the dimensions and material properties of the test brush seal.

Table 1 Geometry and material properties of 20 shoe-brush seal

Physical Properties	SI unit	US unit
Disk diameter	162.9 mm	6.439 inch
Pad length	3.2 mm	0.125 inch
Number of pads	20	
Pad arc length	18 °	
Pad mass, m_P	1.34 gram	0.047 ounces
Pad length	24.69 mm	0.972 in
Bristle diameter, d_b	0.05334 mm	0.0021 in
Bristle free length, L_b	10.114 mm	0.3982 in
Bristle lay angle	42.5 °	
Bristle modulus of elasticity, E	22.48 x 10^5bar	32.6 x 10^6 psi
Bristle Density (circumference)	1350 bristle/cm	3500 bristle/in

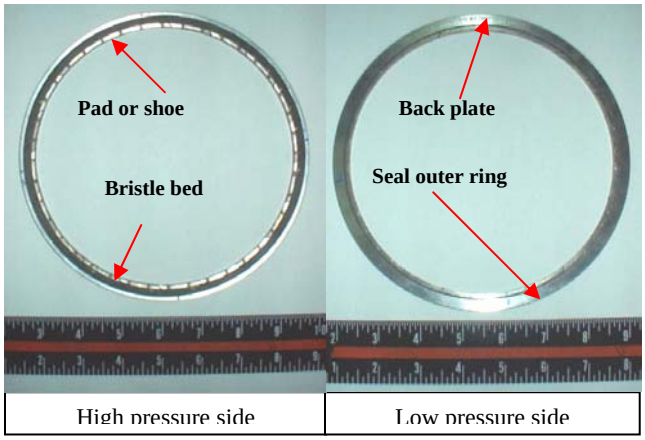

PHYSICAL MODEL, TEST PROCEDURE AND EXPERIMENTAL RESULTS

Static and dynamic load experiments aimed to characterize the structural properties of the test seal were conducted with no shaft rotation and at room temperature (23 °C). A physical model for estimating the structural stiffness coefficient and energy dissipation characteristics of the test shoed brush seal follows. Figure 3 depicts the physical test system and the equivalent 1-DOF translational system. The test system motions are confined to frequencies around its fundamental elastic mode, and hence the simplification to a simple 1-DOF model is plausible. Furthermore, the dynamic response of the test system shows negligible cross-coupling effects; i.e. motions in the orthogonal direction to the applied load are considerably smaller (one order of magnitude) than those recorded in the direction of the excitation force.

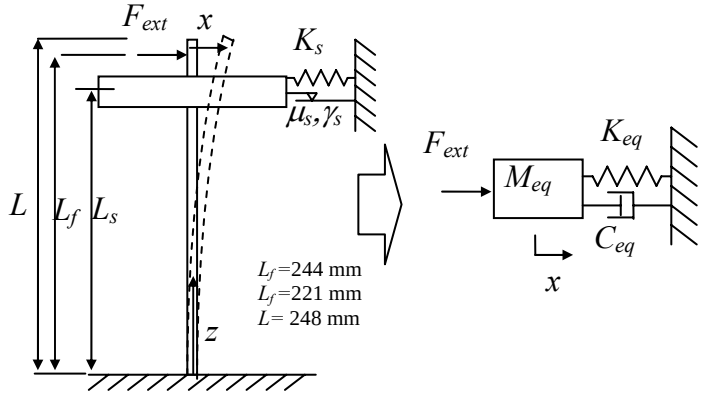

Fig. 3 Schematic view of test system and representation of equivalent mechanical system

The equation of motion of the test system undergoing unidirectional motions is

$$M_{eq}\,\ddot{x} + K_{eq}\,x + C_{eq}\,\dot{x} = F_{ext} \tag{1}$$

where (K_{eq}, M_{eq} , C_{eq}) are the system equivalent stiffness, mass and viscous damping coefficients, respectively. The equivalent stiffness (K_{eq}) and mass (M_{eq}) are determined at

location L_f, where the external load is applied and displacements and accelerations recorded.

The system potential energy and kinetic energy are expressed in terms of the energies for each system component. The fundamental mode shape $\psi(z) = \frac{\left(3Lz^2 - z^3\right)}{2L^3}$ for a cantilever beam, as derived from a static load applied at its free end [10], allows to express the system equivalent stiffness and mass as

$$K_{eq} = K_{shaft} + K_s \left(\frac{\psi(L_s)}{\psi(L_f)} \right)^2 ; M_{eq} = M_D \left(\frac{\psi(L_s)}{\psi(L_f)} \right)^2 + \int_0^L \rho A \psi(z)^2 \, dz \tag{2}$$

where K_{shaft} and K_s represent the shaft[1] and brush seal stiffness coefficients, respectively; M_D is the aluminum disk mass (1.36 kg); and (ρ, A) denote the shaft density and cross-sectional area.

Impact loads and static loads exerted on the disk before installing the brush seal served to identify the baseline parameters of the test rig. The static load experiments consist in pulling the disk with calibrated weights through a rope and pulley system and recording the shaft deflection. An impact hammer was used to hit the disk and the ensuing disk motions were recorded. The natural frequency of the shaft and disk alone is 33 (±1) Hz. Analysis of the transfer function (displacement/load) gives a shaft stiffness (K_{shaft}) of 52 (±2.6) kN/m and a system mass (M_{eq}) equal to 1.18 (±0.05) kg. The shaft stiffness derived from the static load tests equals 53.4 (±0.3) kN/m. The system motion due to the impacts shows very little damping (damping ratio ~ 0.001).

The brush seal was installed and secured atop the vessel. The assembly interference with the disk equals 0.890 mm (diametral). Impact load tests show that the damped natural frequency of the system increases to 53 Hz and the disc motions are well damped.

[1]The shaft stiffness calculated from $K_{shaft} = \int_0^L EI \left(\frac{\partial^2 \psi(z)}{\partial z^2} \right)^2 dz$ yields 54 (kN/m), a value within 2% of the experimental result.

The brush seal stiffens the system and adds substantial damping. Static load tests with the brush seal in place were conducted for multiple sets of pull loads. These tests are divided into tapping and non-tapping, following a method detailed in [8]. The procedures of tapping and non tapping on the seal disk aid to reveal the effects of dry friction and hysteresis arising from the bristle-to-bristle interactions. Thus, two limiting values of test system static stiffness (K_{eq}) are estimated and equal to 125 (±4) kN/m and 176 (±7) kN/m for the tapping and non-tapping conditions, respectively.

The resulting range of stiffness for the brush seal alone (K_s) as derived from the equivalent system stiffness magnitude is 100 (±5) kN/m to 170 (±8) kN/m, and which encloses the value of seal stiffness obtained from dynamic load tests (132 kN/m), as presented later in the analysis of the dynamic load data.

Single frequency dynamic load tests were conducted, from 25 to 100 Hz, and for four force amplitudes. Tests at frequencies below 25 Hz were not performed to avoid the influence of the shaker soft mount natural frequency at ~ 10 Hz. The maximum force amplitude (48 N) was set not to exceed the assembly interference (0.89 mm) for excitations at the system natural frequency, thus avoiding loss of contact between the brush seal shoes and disk. The lowest force amplitude (35 N) is the minimum load able to induce measurable (repeatable) disk motions, i.e. the force necessary to overcome the inherent dry friction of the test seal element. Additional experiments with intermediate force amplitude (44 N) were conducted over a wider frequency range extending from 30 Hz to 300 Hz.

Figure 4 shows the disk amplitude of motion synchronous with the frequency of the applied load. The experiments were conducted with single frequency loads ranging from 25 Hz to 95 Hz. Note that the amplitude of applied load remained fixed while its

frequency varied. There is a threshold force (<40 N) below which the system does not show a resonance peak at the damped natural frequency of 53 Hz. The threshold force is related to the transition from a stick-slip motion regime into a macro slip motion regime, as shown below. Importantly enough, for load amplitudes of 44 N and 48N, the recorded displacements show a nonlinear effect since at the resonant frequency, a difference in load of just 4 N, produces a large change (0.30 mm) in amplitude.

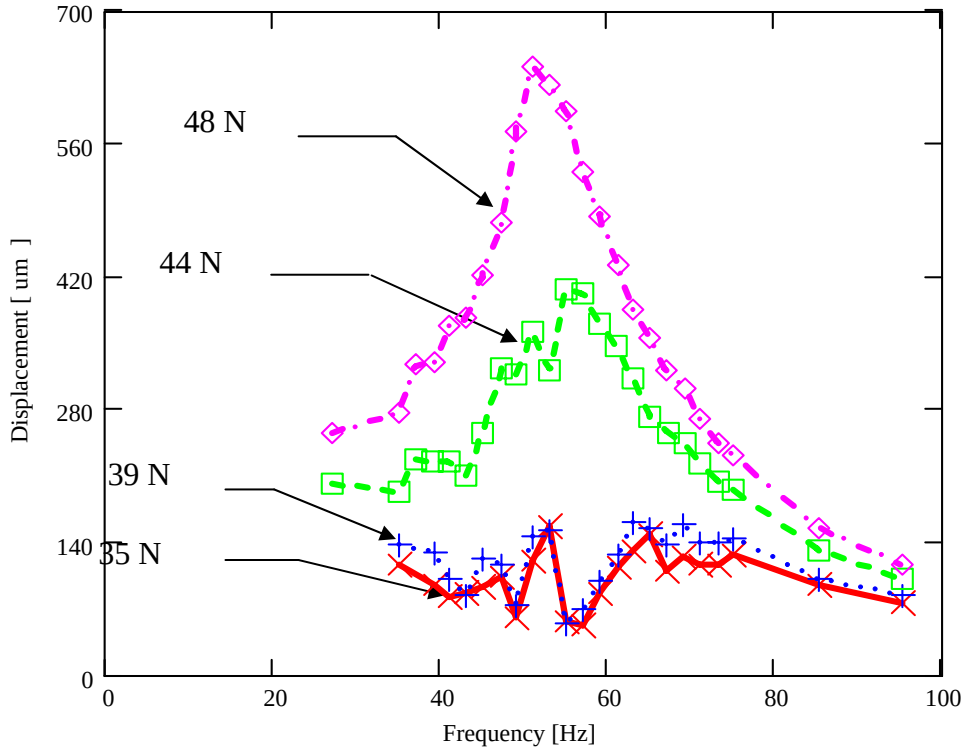

Fig. 4 Measured amplitude of motion (|*X*|) synchronous with dynamic load excitation frequency. Test load magnitudes noted

Figures 5 and 6 depict waterfall plots of the disk displacement and acceleration due to excitation forces with amplitude equal to 35 N and 44 N, respectively. The horizontal axes show the frequency content of the measured displacement or acceleration with amplitudes given in the vertical axis. The excitation frequencies are noted in the inward axis. The vertical scales in Figures 5 and 6 are different.

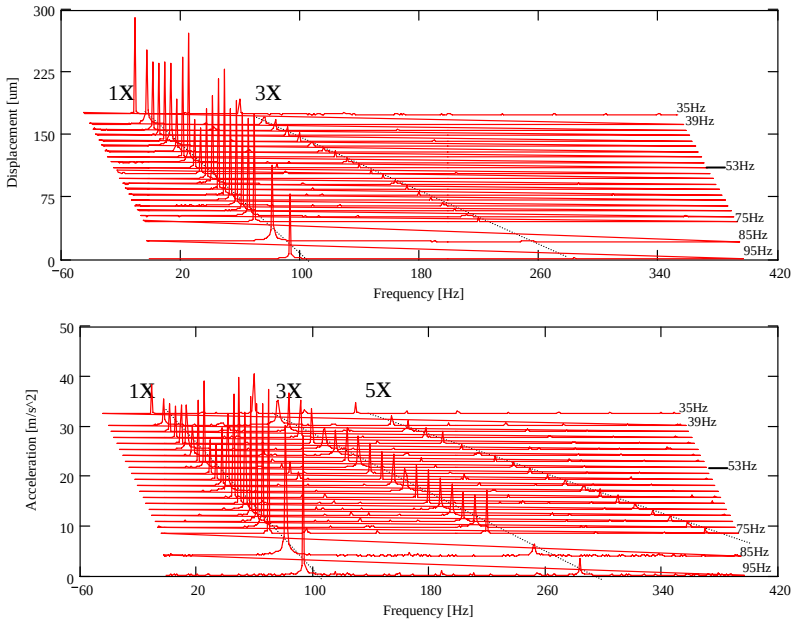

Fig. 5 Waterfall Plot of recorded displacement and acceleration responses due to a external harmonic load (35 N). Frequency range (35 Hz- 95 Hz)

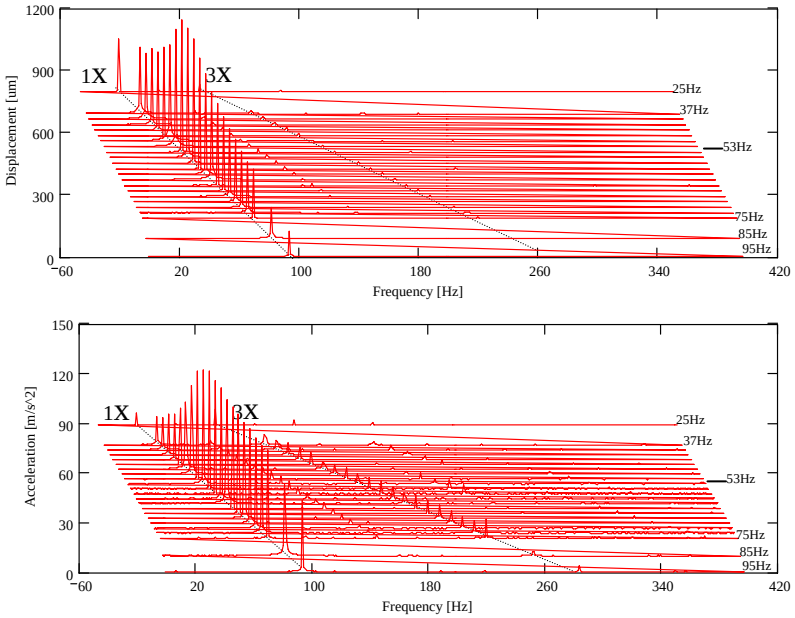

Fig. 6 Waterfall Plot of recorded displacement and acceleration responses due to a external harmonic load (48 N). Frequency range (25 Hz - 95 Hz)

For the large load (48 N), the disk motions are large and mainly synchronous with the excitation frequency. For the 35 Newton load, on the other hand, the disk amplitudes are considerably smaller (up to 75%) and do not evidence a resonance peak as is apparent in Figure 4 for the larger load condition. Furthermore, for the low load, the disk motions, in particular its acceleration, show harmonic components (*3X, 5X*) that are characteristic of a mechanical system with dry-friction. In particular, the *3X* acceleration amplitudes are comparable in magnitude to the synchronous components. Appendix A depicts the time traces of displacement and acceleration versus applied load for excitation frequencies below, at and above the damped natural frequency.

The analysis of the test results shows that, for loads less than 40 N, the disk motion corresponds to a non-linear micro stick-slip regime, where the dry friction force is not constant. As the load amplitude increases, the seal response transitions into a macro-slip regime, where the motion is linear and the friction force is nearly constant in amplitude.

The applied force is periodic and the seal motion (*x)* is also regarded as single-frequency, i.e.

$$x = \mathbf{X}e^{i\omega t}, F_{ext} = \mathbf{F}e^{i\omega t} \tag{3}$$

This last consideration applies only to motions recorded for loads with magnitudes larger than 44 N. Substitution of (3) into (1) gives the complex impedance (**Z***)* function

$$\mathbf{Z} = \frac{\mathbf{F}}{\mathbf{X}} = (K_{eq} - \omega^2 M_{eq}) + i\,\omega\, C_{eq} \tag{4}$$

The test system stiffness (K_{eq}) and mass (M_{eq}) can be readily obtained from $K_{eq} - M_{eq}\omega^2 = \mathbf{Re}(\mathbf{Z})$ over a pre-defined frequency range.

The motion of the brush bristles under bending and the dry friction arising from bristle-to-bristle and bristles-to-back plate interactions determines the seal dynamic

forced response. The energy dissipation mechanism is clearly not of viscous type. Presently, the energy dissipation model assumed comprises of structural[2] and dry friction damping mechanisms. Thus, the energy dissipated in one period of seal motion is [12]

$$E_{dis} = \gamma_{eq} \pi K_{eq} \left|\mathbf{X}\right|^2 + 4\mu \left|\mathbf{F}\right|\left|\mathbf{X}\right| \tag{5}$$

The coefficients γ_{eq} and μ represent a structural loss coefficient and dry friction coefficient, respectively. The brush seal loss parameter, γ_s, equals

$$\gamma_s = \gamma_{eq} \frac{K_{eq}}{K_s} \left(\frac{\psi(L_f)}{\psi(L_s)} \right)^2 \tag{6}$$

The dissipated energy must equal to the work performed by the applied external force

$$W = \oint F_{ext} \dot{x} dt \tag{7}$$

For completeness, the dissipated energy for damping of the viscous type [10] is

$$E_{dis} = \pi \omega C_{eq} \left|\mathbf{X}\right|^2 \tag{8}$$

where the equivalent viscous damping coefficient (C_{eq}) equals

$$C_{eq} = \frac{\gamma_{eq} K_{eq}}{\omega} + \frac{4\mu \left|\mathbf{F}\right|}{\pi \omega \left|\mathbf{X}\right|} \tag{9}$$

Note that this equivalent coefficient is frequency and amplitude (load and motion) dependent. Algebraic manipulation of Eqn. (4) gives

$$\left(\left(1 - \left(\frac{\omega}{\omega_n} \right)^2 \right) + {\gamma_{eq}}^2 \right) \left|\mathbf{X}\right|^2 + \left(\frac{8\mu \left|\mathbf{F}\right|}{\pi K_{eq}} \gamma_{eq} \right) \left|\mathbf{X}\right| - \left(\left(\frac{\left|\mathbf{F}\right|}{K_{eq}} \right)^2 \left(1 - \left(\frac{4\mu}{\pi} \right)^2 \right) \right) = 0 \tag{10}$$

With a physical solution for the motion amplitude given by

$$\left|\mathbf{X}\right| = \frac{\left|\mathbf{F}\right|}{K_{eq}} \left[\frac{-\left(\lambda \gamma_{eq}\right) + \sqrt{\left(1-\lambda^2\right)\left(1-r^2\right)^2 + {\gamma_{eq}}^2}}{\left(\left(1-r^2\right)^2 + {\gamma_{eq}}^2\right)} \right] \tag{11}$$

[2] Energy dissipated internally within the material itself due to cyclical stresses [11].

where $\lambda=4\mu/\pi$ and $r=\omega/\omega_n$ is afrequency ratio. In the tests, the load and motion amplitude are recorded, i.e. |**F**| and |**X**|. Thus, a nonlinear curve-fit, following Eqn. (11), is applied to the test data to determine the energy dissipation parameters, γ_{eq} and μ, over a frequency range. Table 2 lists the results of the identification procedure.

Table 2 Test system and brush seal identified parameters from dynamic load tests (Load 48 N, 25 Hz to 95 Hz)

Parameters	Equivalent system	**Brush seal alone**
Stiffness [kN/m]	143	**132**
R^2	0.99	
Dry Friction coefficient, μ		**0.55**
Loss Factor coefficient, γ	0.16	**0.19**
R^2	0.97	

R^2: correlation coefficient representing goodness of curve fit to test data

The magnitudes found for the brush seal energy dissipation parameters, γ_s and μ, are considered reasonable when considering the complicated motions of the bristle-to-bristle interactions and bristles rubbing against the back plate.

Figure 7 depicts the recorded and model derived amplitude of response versus frequency. The force of magnitude 48 N is kept constant throughout the frequency span. The model predictions reproduce Eqn. (11) with the identified system parameters given in Table 2.

Figure 8 shows the dynamic stiffness (real part of the test impedance function, **Re(Z),** versus frequency and model results based on the formulae K_{eq}-$M_{eq}\omega^2$. The graph includes curves for the dynamic stiffness derived using the maximum and minimum stiffness obtained from the static load tests[3]. The estimated stiffness coefficient (K_{eq}) from the dynamic load tests lies within the minimum and maximum static stiffness values.

[3] Static tests on the shoed brush seal render two stiffness values, with and without including the stiffening effect of the dry friction interaction on the seal. As the test system is statically loaded, when tapping on the disk the system is perturbed "to break" the friction interaction between the bristles [8].

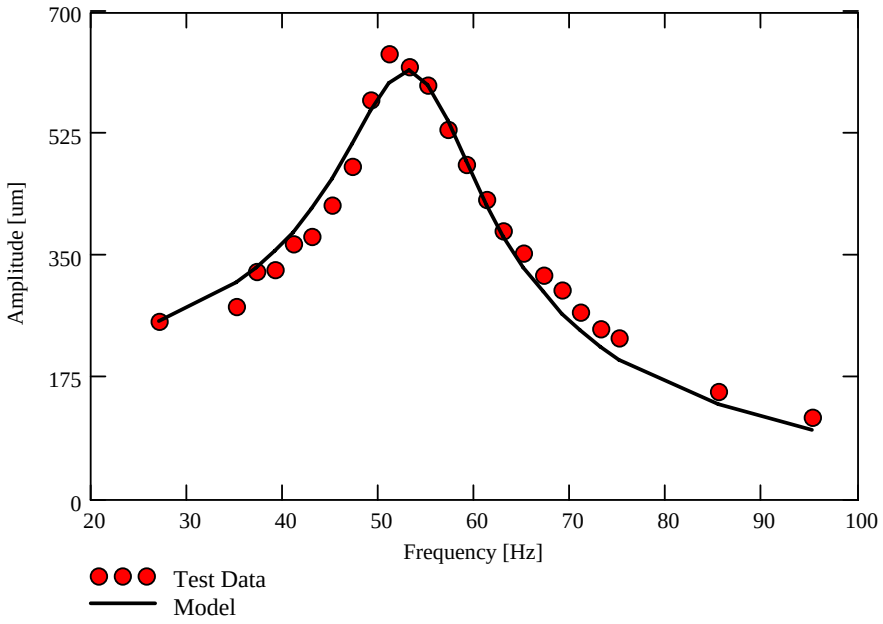

Fig. 7 Amplitude of synchronous motion versus frequency. Load magnitude = 48 N. Correlation of model predictions to test results

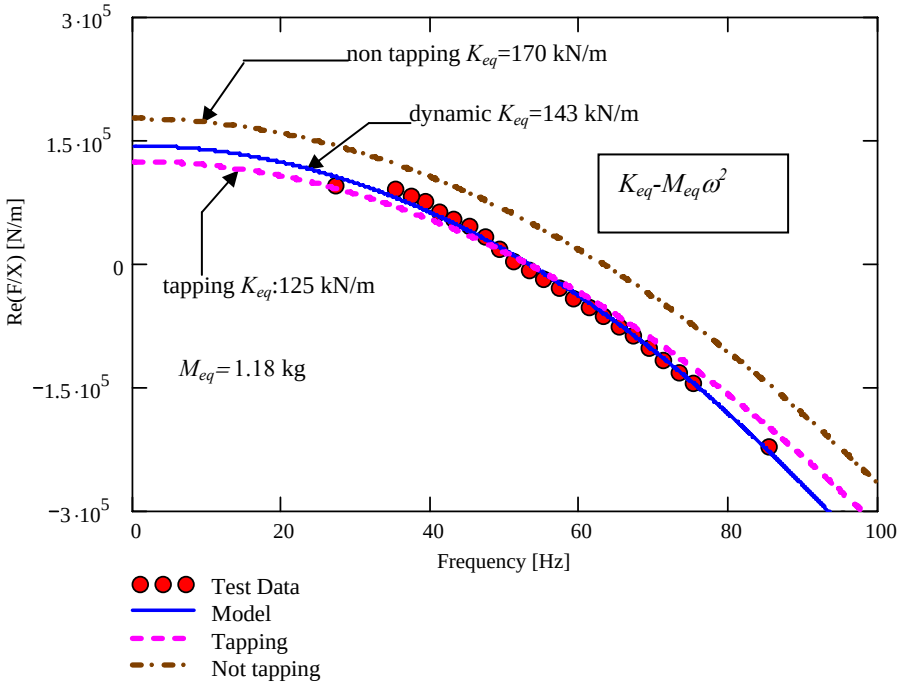

Fig. 8 Test system identified dynamic stiffness versus frequency. Load magnitude = 48 N. Model predictions based on $K_{eq} - M_{eq}\omega^2$. Curves derived from stiffnesses obtained from taping and non-tapping static load tests also shown

Figure 9 shows the phase angle between the displacement response and the excitation force. The phase angle is fairly constant for frequencies away from the natural frequency. Most importantly, at very low frequencies the constant phase lag between the system motion and the excitation force evidences the predominant effect of dry friction. Note that the model predictions reproduce well the test data. This is notable since the curve-fit of the amplitude of motion vs. frequency, Eqn (11), does not convey information on the phase angle.

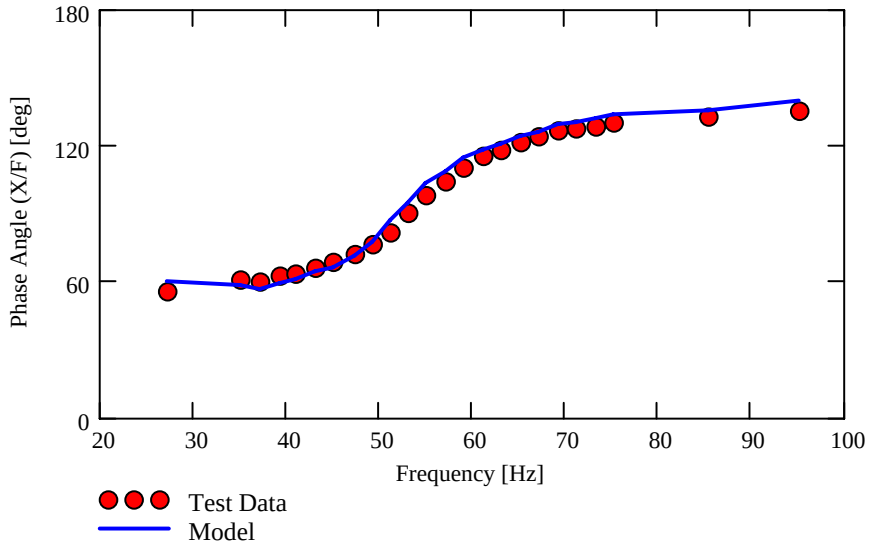

Fig. 9 Phase angle lag between displacement response and excitation force versus frequency. Load amplitude (48N)

Figures 10 and 11 show the energy dissipated (=work) by the test system in one period of motion for forces of 48 N and 44 N, respectively. The model predictions, equation (5), are based on the identified parameters given in Table 2. Note that for the load=44 N, the tests were conducted over a larger frequency range, i.e. to 300 Hz. The results shown in Figure 11 demonstrate that the identified parameters render accurate predictions over a broader frequency rage, i.e. 30 Hz to 200 Hz. The shaded area above 240 Hz, encloses the second natural frequency of the test rig system. Thus, the identified

dry friction (μ) or the structural loss (γ) coefficients are rather independent of the excitation frequency.

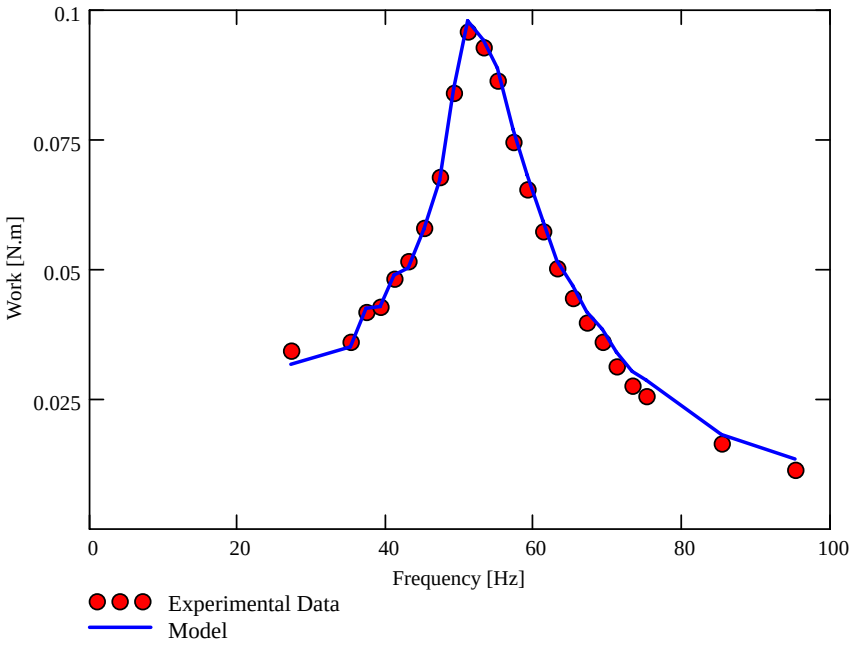

Fig. 10 Work=Energy dissipated by test system versus frequency for one period of motion. External load (48 N) on frequency range 25-95 Hz

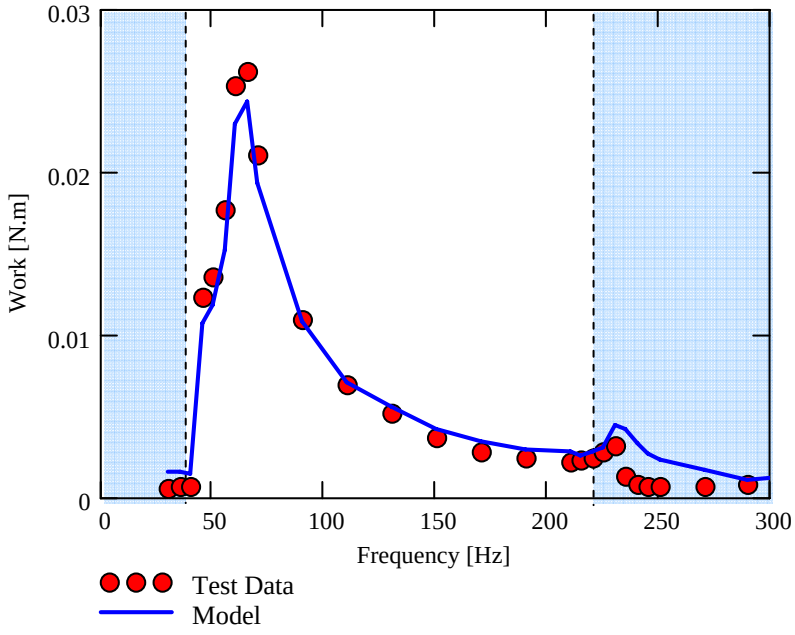

Fig. 11 Work=Energy dissipated by test system versus frequency for one period of motion. External load (44 N) on frequency range 30-300 Hz

Figure 12 shows the equivalent viscous damping (C_{eq}) versus frequency. The test data is extracted from Im(Z)/ω while the model results reproduce Eqn. (9) using the identified parameters. The model presents good agreement with the experimental data in the range 25-60 Hz. For higher frequencies, the model overpredicts (up to 20 %) the test system equivalent damping. Most importantly, note that the lowest viscous damping magnitude occurs at the natural frequency of the test system. At low frequencies, the viscous damping evidences the effect of dry-friction.

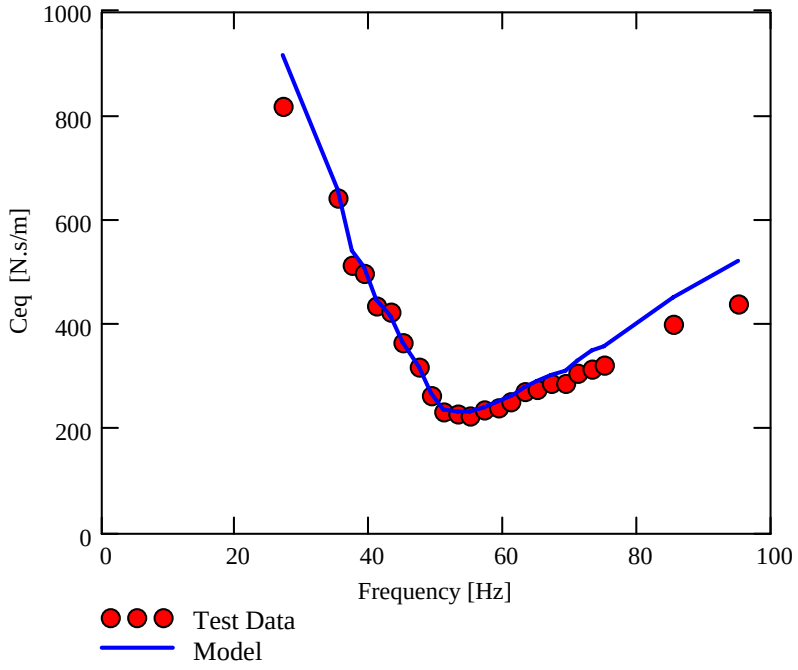

Fig. 12 Equivalent viscous damping coefficient of test system. External load (48 N) on frequency range 25-95 Hz. Test data and model results

SEAL LEAKAGE MEASUREMENTS AND PREDICTIONS

Measurements of leakage through the test seal were conducted for increasing air pressures at ambient conditions. Recall that these measurements are without the shaft spinning. The measured flow rates are correlated to predictions based on a semi-empirical

leakage model advanced by Chupp and Holle [12]. An EXCEL® VB program contains the model in [12] as detailed by San Andrés [13].

Table 3 shows the geometry and operating conditions for the test shoed brush seal. A turbine flowmeter (± 0.2 SCFM) and a strain gage sensor (± 0.5%) record the flow rate and upstream pressure measurements, respectively.

Table 3 Brush seal leakage model inputs and flow conditions

Physical parameters		
0.0533	Bristle diameter(d_b)	(mm)
42.5	Lay angle(γ)	deg
3500	Bristle density /inch(N)	circumference
163.6	Rotor diameter(D_j)	(mm)
177.8	Upstream diameter(D_u)	(mm) retainer plate
3.175	Seal width(L)	(mm)
Flow conditions		
1.01	Downstream Pressure (P_d)	(bar)
14.7		(psia)
1.01 to 3.25	Upstream Pressure (P_u)	(bar)
15.4 to 49.4		(psia)
22 to 25.5	Upstream Temperature (T_u)	(^{0}C)
Air		
287.05	Gas constant(R)	(J)/(kg K)

Figure 13 presents the measured leakage or mass flow rate ($\dot{m}$) versus the pressure ratio (p_r=$P_u P_s$) and the leakage flow model predictions using a uniform effective thickness (B=0.437 mm [17 mils]) [12]. The effective thickness (B) is an empirical parameter that the model relies on. The selected B renders best correlation to the experimental data at (p_r) ~ 2.5.

Brush seal analysis also relies on a flow factor (Φ) or generalized leakage parameter that allows comparing the performance of brush seals of any size [12]. The flow factor (Φ) [$\frac{g\sqrt{^0K}}{N\ s}$], a function of the upstream to downstream pressure ratio (p_r), equals [12]

$$\Phi = \frac{\dot{m}\sqrt{T_u + 273.5}}{P_u\ A_u} \tag{12}$$

where A_u is the seal upstream area, $\dot{m}$ is the leakage in g/s, and (P_u, T_u) are the upstream pressure and temperature conditions. Figure 14 depicts the calculated flow factor and the one derived from the measurements versus the supply to discharge pressure ratio. The

correlation is rather poor since the magnitudes of measured flow rate demonstrate laminar flow operation.

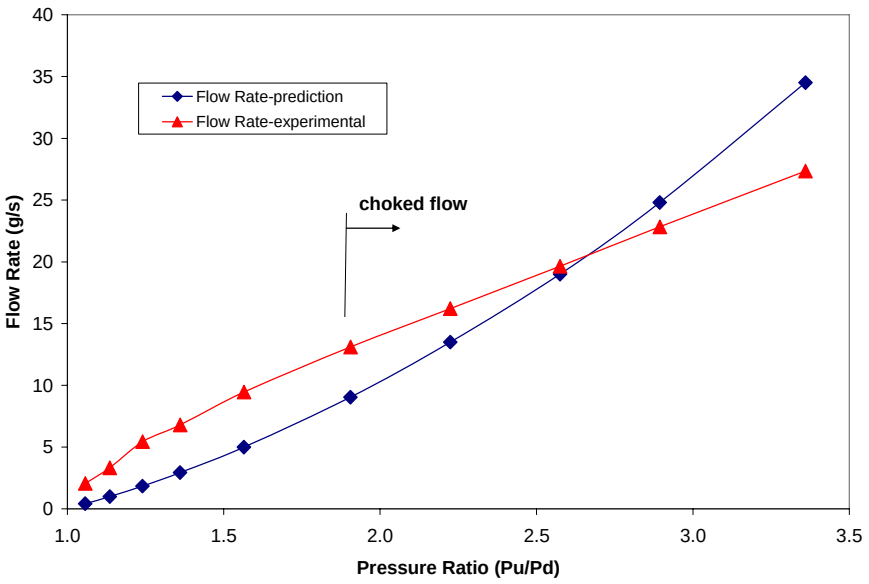

Fig. 13 Measured and predicted leakage for test shoed brush seal versus pressure ratio. Predictions based on uniform effective thickness (*B*=0.437 mm)

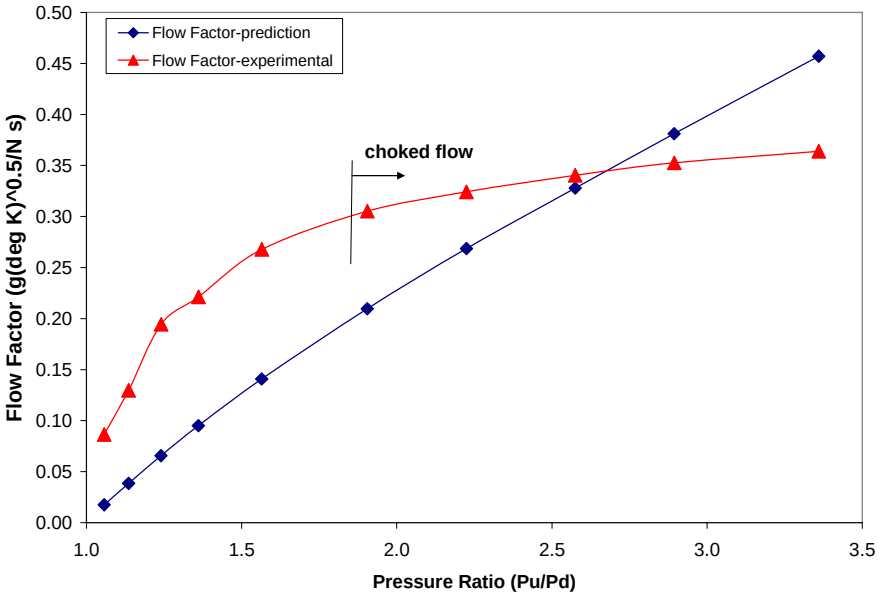

Fig. 14 Brush seal experimental and predicted flow factor versus pressure ratio. Uniform effective thickness (*B*=0.437 mm)

Brush seal manufacturers, e.g. [7], also characterize brush seal leakage performance in terms of an effective clearance (c_E) that represents a film thickness equivalent to that of a corresponding "one sharp tooth" labyrinth seal. The clearance (c_E), a function of an orifice flow factor, is defined as

$$c_E = \frac{\dot{m}\sqrt{(T+273.15)}}{P_u \pi D \varphi} \tag{13}$$

$$\varphi = \begin{cases} \sqrt{\frac{\gamma}{R}}\sqrt{\frac{2}{\gamma-1}P_R^{\frac{-(\gamma+1)}{\gamma}}(P_R^{\frac{(\gamma-1)}{\gamma}}-1)} & P_R \le P_{choke} \\ \sqrt{\frac{\gamma}{R}}\sqrt{\frac{2}{\gamma+1}}\left(\frac{2}{\gamma+1}\right)^{\frac{1}{\gamma-1}} & P_R > P_{choke} \end{cases} \quad ; P_{choke} = \left(\frac{2}{\gamma+1}\right)^{\frac{-\gamma}{\gamma-1}} = 1.89 \tag{14}$$

with γ=1.4 denotes the gas (air) ratio of specific heats.

Figure 15 shows the calculated effective "labyrinth seal" clearance and predictions derived from the laminar flow model. versus pressure ratio. The average predicted clearance is 0.042 mm (1.65 mil), while the one derived from the flow measurements increases to 0.067 mm (2.63 mil) at the largest pressure tested. Note that the shoed brush seal shows a 200 % increase in effective clearance over the pressure range tested. The change is due to the "opening" of the seal pads being pushed away from the shaft as the pressure upstream increases.

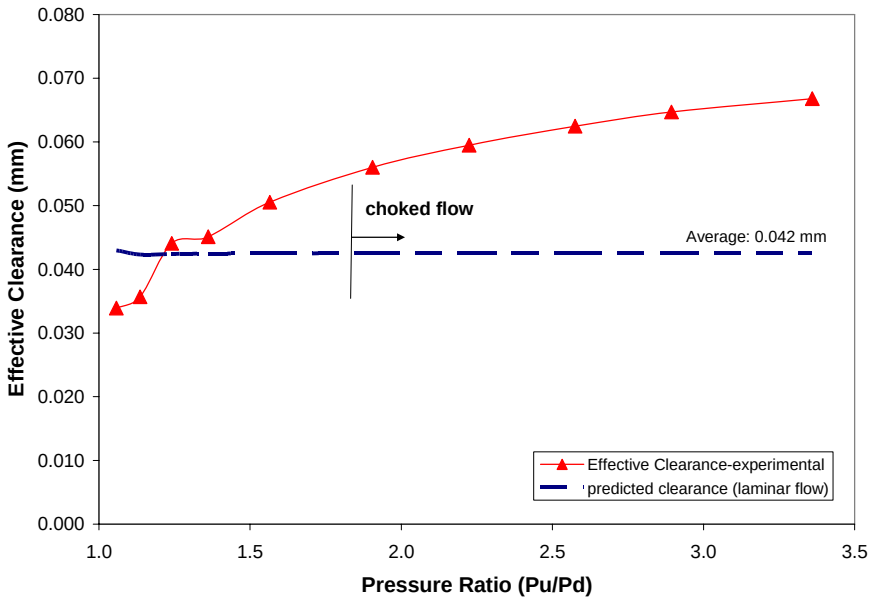

Fig. 15 Equivalent "labyrinth seal" clearance for test brush seal, from leakage measurements and predictions based on laminar flow model (c_E=0.042 mm)

CONCLUSIONS

The report presents experimental results and a procedure for estimation of the structural stiffness and damping characteristics of a 20-pad shoed brush seal. The simple test rig comprises of a non-rotating cantilever shaft with a solid disk at its free end. The test brush seal is mounted with an interference fit to the disk. An electromagnetic shaker, softly mounted, delivers a single-frequency load of constant magnitude into the shaft free end and ensuing disk displacement and acceleration are recorded. The shaft stiffness and system equivalent mass are determined experimentally prior to installation of the test seal. The static structural stiffness of the test seal is not unique since it depends on whether the procedure allows for stick or slip to occur. The stick/slip phenomenon, characteristic of systems with dry-friction, is due to the bristle-to-bristle and bristles-back plate interactions. Thus, two seal static stiffnesses (maximum and minimum) are reported.

In the dynamic load tests, a force of certain amplitude is needed to overcome the micro stick/slip regime and to bring the seal motions into a macro-slip regime. In the identification procedure conducted in the frequency domain, the stiffness and mass coefficients are readily obtained from the real part of the system impedance. The brush-seal energy dissipation mechanism is modeled as a combination of structural and Coulomb damping, i.e. represented by a structural loss factor (γ_s) and a dry friction coefficient (μ). These coefficients are identified in the frequency range from 25 Hz to 95 Hz, enclosing the test system natural frequency (53 Hz). Model predictions based on the identified parameters (γ_s=0.55, μ=0.19) reproduce very well the measured amplitude of motion and energy dissipated, even for frequencies higher than the largest in the identification range.

Experimental characterization of the shoed brush seal energy dissipation features is crucial for predictions and validation of its rotordynamic coefficients. Current experimentation includes similar tests being conducted with increasing pressure drops across the brush seal.

Measurements of the leakage through the seal as the supply pressure increased show the seal unique performance characteristics, i.e. very small flow rate which can be effectively represented as a "labyrinth seal" of very narrow clearance.

ACKNOWLEDGEMENTS

The authors thank Mr. John Justak from Advanced Technology Group, Inc. for providing the shoe brush seal (www.advancedtg.com)

REFERENCES

[1] Chupp, R., Raymond, E., and Nelson, P., 1995, "Evaluation of Brush Seals for Limited-Life Engines," AIAA Journal of Propulsion and Power, **9**, pp. 113-119.

[2] Fellenstein, J. A., DellaCorte, C., 1996, "A New Tribological Test for Candidate Brush Seal Material Evaluation," Tribology Transactions, **39**, pp. 173-179.

[3] Conner, J. K., and Childs, D., 1993, "Rotordynamic Coefficient Test Results for a Four-Stage Brush Seal," AIAA Journal of Propulsion and Power, **9**, pp. 462-465.

[4] Childs, D., and Vance, J. M., 1997, "Annular Gas and Rotordynamics of Compressors and Turbines," Proceedings of the 26th Turbomachinery Symposium, pp. 201-220.

[5] Hendrics, R. C., Csavina, K. R., Griffin, T. A., Kline, T. R., Pancholi, A., Sood, D., 1994, " Relative Comparison Between Baseline Labyrinth and Dual Brush Compressor Discharge Seals in a T-700 Engine Test," ASME PAPER 94-GT - 266.

[6] Justak, J., 2000, "Hybrid Brush Seal Capable of Reverse Rotation," Proposal to NAVY SBIR Program, Advance Turbomachinery Solutions, Miami, Fla.

[7] Justak, J., 2002, "Hybrid Brush Seal Capable of Reverse Rotation," Technical Report, Navy SBIR Phase II Project, Advanced Turbomachinery Solutions, Miami, FL., April.

[8] Delgado, A., San Andrés, L., Justak, J., 2003, "Identification of Stiffness and Damping Coefficients in a Shoed Brush Seal," Proceedings of the VII Congreso y Exposición Latinoamericana de Turbomaquinaria, Veracruz, Mexico, October.

[9] Delgado, A., San Andrés, L., Justak, J., 2004, "Analysis of Performance and Rotordynamic Force Coefficients of Brush Seals with Reverse Rotation Ability,"

ASME PAPER GT 2004-53614.

[10] Spotts, M. F., Shoup, T. E., 1998, “Design of Machine Elements,” *Prentice Hall, Inc.,* NJ, pp. 39-42.

[11] Thomson, W. T., 1998, “Theory of Vibration with Applications,” *Prentice Hall, Inc*., NJ, pp. 72-74

[12] Ginsberg, J. H., 2001, “Mechanical and Structural Vibrations,” *John Wiley & Sons, Inc*., NY, pp. 135-139

[13] Chupp, R. E., and Holle, G. F.,1996, “Generalizing Circular Brush Seal Leakage Through a Randomly Distributed Bristle Bed,” ASME Journal of Turbomachinery, **118**, pp.153-161

[14] San Andrés, L., 2003, “Analysis of Performance and Rotordynamic Force Coefficients of Brush Seals with Reverse Rotation Ability,” Final Report to Advanced Turbomachinery Solutions (ATS), March 2003. (Computational Program)

APPENDIX A. Time domain experimental data

Typical time-displacement and acceleration versus applied load are shown below for two load conditions with 35 N and 48 N amplitudes. The excitation frequencies noted correspond to magnitudes below, at and above the damped natural frequency of the test system.

The graphs include the synchronous component of motion as determined from the Fourier analysis of the recorded time data for force and motions. In general, the lowest number of periods recorded in a test equals 15. Note the difference in scales for the displacements and accelerations due to loads equal to 35 N and 44 N.

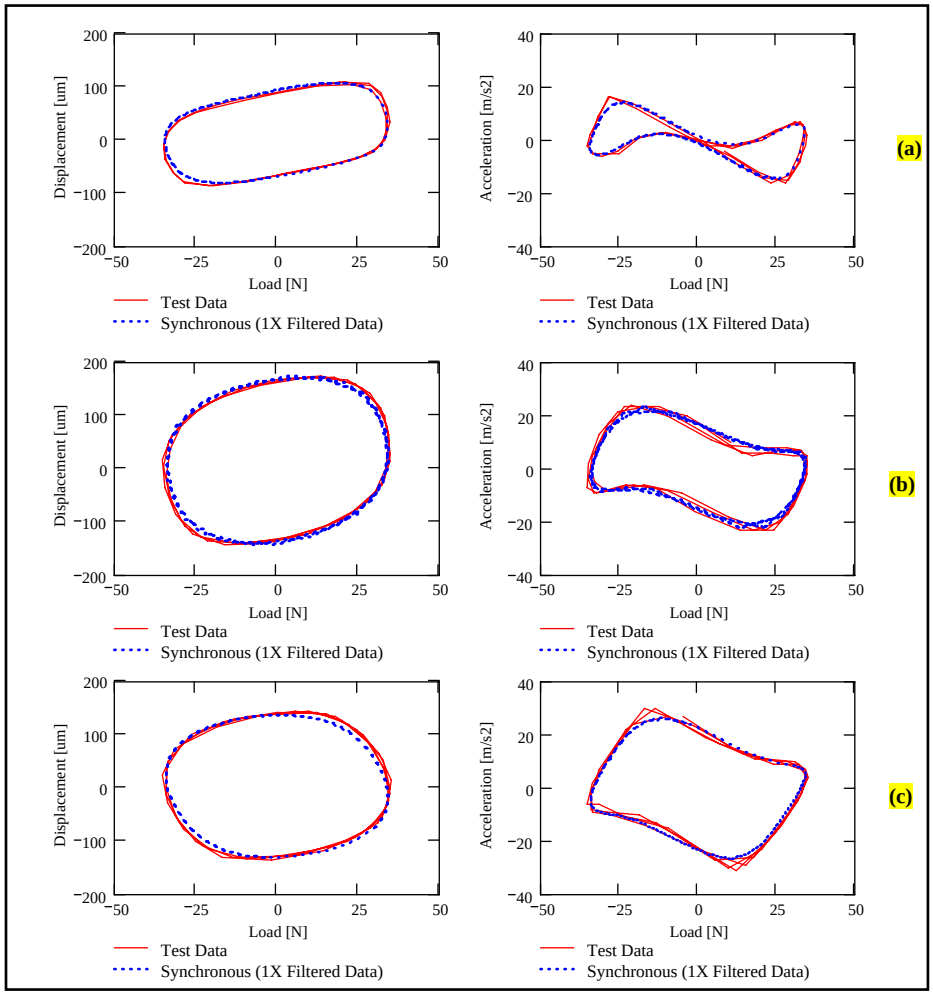

Fig A.1 Displacement and acceleration vs. external load (35 N) for excitation frequency equal to (a) 43 Hz, (b) 53 Hz, and (c) 63 Hz

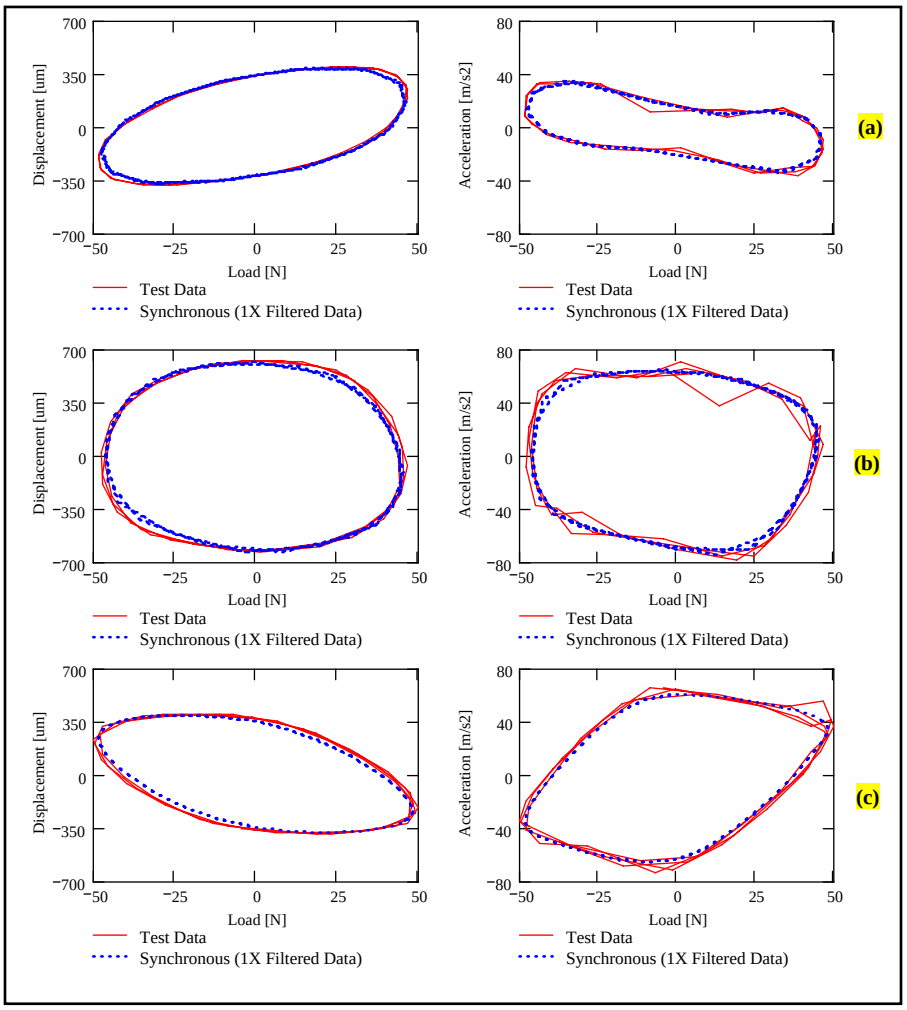

Fig. A.2 Displacement and acceleration vs. external load (44 N) for excitation frequency equal to (a) 43 Hz, (b) 53 Hz, and (c) 63 Hz